Supporting Information: Background-Suppressed High-Throughput Mid-Infrared Photothermal Microscopy via Pupil Engineering

Haonan Zong,[†,¶] Celalettin Yurdakul,[†,¶] Yeran Bai,[†] Meng Zhang,[‡] M. Selim Ünlü,[*,†,‡] and Ji-Xin Cheng[*,†,‡]

†*Department of Electrical and Computer Engineering, Boston University, Boston, MA 02215, USA*

‡*Department of Biomedical Engineering, Boston University, Boston, MA 02215, USA*

¶*Contributed equally to this work.*

E-mail: selim@bu.edu; jxcheng@bu.edu

1 Temperature dependence of photothermal signal

Since the scattering signal is differentiable in the temperature domain, we can write the derivative of the scattered field E_{scat} as follows:

$$\lim_{\Delta T \to 0} \Delta T \frac{dE_{scat}(T)}{dT} = E_{scat}(T + \Delta T) - E_{scat}(T) \tag{1}$$

In our system, the infrared (IR) absorption induced the temperature change is less than 5 K for a 500 nm PMMA bead. Also, we numerically demonstrate that the scattered field modulation depth ($\Delta E/E$) for a 1 K temperature increase is about 10^{-4}. This modulation

depth is determined by the sample's thermo-optic and thermal-expansion coefficients. Applying the chain rule on eq. 1, the modulation depth for $|\Delta E| \ll |E|$ can be written in a linear form,

$$\frac{\Delta E}{E} = \Delta T \frac{dE_{scat}(T)}{dT} = \Delta T \left[\frac{\partial E_{scat}(r,n)}{\partial r} \frac{dr}{dT} + \frac{\partial E_{scat}(r,n)}{\partial n} \frac{dn}{dT} \right] \tag{2}$$

Together, our assumption in eq. 2 holds true for small temperature changes owing to the sample's linear temperature response and very small thermal coefficients in the -4 orders of magnitude at the room temperature.[S1] The simulated photothermal response curve as a function of ΔT is shown in Figure S2. We point out that this linearity breaks at the large temperature changes of ΔT >30 K. This stems from the fact that the photothermal effect induces the strong change in the scattered field. That is to say, the modulation depth should be within the range of 0.01 for the assumption of the scattered field's linear temperature dependence. Otherwise, the modulation depth-dependent temperature change calculations can be performed by polynomial curve fitting to the theoretical findings.

2 Backside infrared illumination optimization

To improve the transmission on silicon, we illuminate the substrate at close to the Brewster angle. The default IR beam output is linearly polarized along the z-axis which is defined as s polarization state. We topologically rotate the s polarized IR light to p polarized state using two 45 ° gold mirrors as shown in Figure S4. The first mirror reflects the light along the z-axis (vertical). The second mirror redirects the beam along the x-axis (horizontal). To set the IR beam height without changing the polarization state, we added two 45 ° gold mirrors facing each other. The arrangement of the mirrors was placed accordingly to this design right after the IR laser output. We achieve an angle of incidence of 61° which goes beyond the objective's acceptance angle of 53°. In a single surface, this oblique illumination provides 84% transmission for p polarization compared with 20% transmission in the initial s

polarization state. With this configuration, we improve the transmission rate overall 4-fold.

3 COMSOL simulation of transient temperature response of pulsed infrared heating

We used COMSOL to simulate the transient temperature rise induced by the pulsed IR absorption. The simulation is compartmentalized into three parts: (1) calculating the sample's absorption cross-section (σ_{abs}), (2) modeling the experimental IR pulse, and (3) simulating the heating process. The absorption cross-section of a beads is calculated using the particle's dielectric and size information. Then, the absorbed power (P_{abs}) of the sample is calculated based on the intensity (I) of the heating beam using the equation $P_{abs} = \sigma_{abs} \cdot I$. To obtain IR intensity in time domain, an approximate representation of the real IR pulse is modeled based on the experimental measurements. Once the time-domain heating power density function is calculated, the transient temperature response can be simulated at the final step. This simulation referenced the steps reported in.[S2]

3.1 Absorption cross-section calculation

In this part, the absorption cross-section of PMMA beads with different sizes at IR wavenumber 1729 cm^{-1} were calculated using COMSOL 5.3a, electromagnetic waves, frequency domain. The geometry diagram is shown in S6. The refractive index of PMMA at 1729 cm^{-1} was taken as 1.5+0.46i.[S3] Since the focused IR spot size (tens of microns) much larger than the sub-micron beads, the incident IR beam can be treated as a plane wave. The electromagnetic wave equation is numerically solved by COMSOL. Then, the absorption cross-section is calculated by $\sigma_{abs} = \frac{1}{I}\iiint_V ewfd.Qe \, \mathrm{d}x \, \mathrm{d}y \, \mathrm{d}z$, where $ewfd.Qe$ is the electrical power loss density. I is the IR intensity that can be assumed to be any finite value since it is normalized. σ_{abs} is independent with the value of I.

The absorption cross-section calculations for different PMMA bead sizes are shown in S7. We cross-validated the COMSOL results with a standard Mie scattering calculation tool

(https:// omlc.org/calc/mie_calc.html). Both results show great agreement with each other. In this simulation, the electromagnetic power loss density distribution, which is the heating power density distribution, is obtained. As shown in S8, the power density distribution is very uniform for a 500 nm bead, which is due to the relatively small size of the bead compared to the wavelength. To simplify the following steps of the simulation, the heating power density used in part (3) is assumed to be uniformly distributed.

3.2 Experimental IR pulse modeling

The real experimental IR pulse used in this study is mathematically modeled. The distribution of the IR intensity in the space domain can be assumed to be a 2D Gaussian function. To find out the distribution, the beam size of the IR is fitted according to the dark-field MIP image of 500 nm PMMA beads. We first found the peak intensity coordinates of 164 beads with SNR larger than 10. Using the 164 (x, y, z) coordinates, which were already shifted to the maximum center position, the least-squares fitting to a 2D Gaussian function was performed as shown in Figure S9. Using the fitting result of the 2D Gaussian function intensity distribution ($y = \alpha e^{-ln(2)\cdot(\frac{x^2}{\sigma_x}+\frac{y^2}{\sigma_y)}}$), the power of the IR beam P and the intensity at center point (α) of the IR beam can be related together by this equation, $\iint\limits_{\infty} \alpha e^{-ln(2)\cdot(\frac{x^2}{\sigma_x}+\frac{y^2}{\sigma_y)}}\,\mathrm{d}x\,\mathrm{d}y = P$, which can be simplified to $\alpha\pi\sigma_x\sigma_y/ln(2) = P$. The IR power P at $1729cm^{-1}$ was measured by a power meter to be 7.8 mW. Thus, the intensity at the center of the beam can be obtained to be $1.4 \times 10^6\, W \cdot m^{-2}$. In the following parts of the simulation, the intensity was chosen to be this beam center value. To simulate the heating process, the time-domain IR pulse needs to be modeled. To do so, we experimentally obtained the IR pulse signal using an MCT (Figure S10a). The IR pulse shape which has 1000 ns pulse width is modeled to be a piecewise function as shown in Figure S10b. The first 200 ns time interval is set to a Gaussian pulse function, and the following 800 ns is set to a linear function. Using the IR beam's intensity profile and repetition rate, the time-dependent intensity function ($I(t)$) of one pulse can be calculated using the aforementioned average intensity.

3.3 Heat dissipation simulation

The heat dissipation of the bead can be simulated using COMSOL 5.3a, heat transfer in solid model. The following heat conduction functions were solved in COMSOL. The simulation result of the temperature distribution is shown in Figure S11. In this simulation, the 500 nm PMMA bead is sitting on the top of a silicon hemisphere. The contact area radius is 0.4 times the bead radius. The top hemisphere is air, and the radii of the air and silicon hemisphere are 40 times larger than the bead radius. The temperature at the PMMA silicon interface and the PMMA air interface is assumed to be continuous. The initial temperature is assumed to be 298 K, and the simulation boundary is assumed to have a 298 K constant temperature. Heat convection is not considered in this simulation. The heat source is set to be the domain of the PMMA bead. The heat source term is set to be $Q(t)$ as shown below.

$$\rho C_p \frac{\partial T}{\partial t} + \nabla \cdot \mathbf{q} = Q \tag{3}$$

$$\mathbf{q} = -k\nabla T \tag{4}$$

where ρ is the density of the material, C_p is the heat capacity at constant pressure, T is temperature, t is time, k is the thermal conductivity. Q is the heat source. $Q(t) = \frac{I(t)\sigma_{abs}}{V}$, V is the volume of the 500 nm PMMA bead. The transient temperature response of the PMMA bead can be obtained. The temperature is calculated from the temperature distribution. To do that, the temperature of the PMMA bead is integrated over its volume followed by volume normalization. Figure S14 shows the transient temperature response of different particle sizes ranging from 50 to 500 nm. These plots are calculated for the pulse parameters discussed in the previous section. It is seen that ΔT decreases with the size since the heat dissipation constant is much faster for smaller particles. Therefore, small nanoparticles require a much shorter IR pulse width.

4 Image acquisition and processing

The automated image acquisition and spectral scans are implemented in custom-written software in Python. This software controls the camera, objective piezo-scanner, pulse generator, and IR-laser via serial communication. The camera and IR laser SDKs are provided by the companies. To account for the laser intensity fluctuations, the camera captured the beam reflected from a mirror placed right after the beam splitter. The reflected beam is directed into the bottom-left edge of the camera field-of-view without obscuring the focused IR spot. To prevent the image saturation at this reference region, the intensity of the reflection is adjusted by an absorptive neutral density filter. Each frame is normalized by the average intensity of all pixels at the reference region. We typically acquire 2000 images in total, 1000 hot and 1000 cold images. The hot and cold frames are recorded sequentially such that the odd- and even-numbered frames refer to hot and cold, respectively. The frames are summed into the corresponding state frame variable followed by averaging. To avoid overflow in summation, the frames are stored as 32 bits. The frame averaging and normalization is performed in real-time which significantly improves the memory and space usage efficiency. That is to say, instead of saving gigs of image data to average during the post-process, only two averaged hot and cold images (a few MBs) are saved on disk. This customized process becomes particularly the importance of hyperspectral image acquisitions in which order of a million images are captured. Note that only in the signal-to-ratio characterization experiment (main text Figure 4f), all images are saved. The hyperspectral images are processed through automated software written in MATLAB. To find the particle locations, we first create a binary image from the dark-field scattered images by simple threshold (typically pixel value $>$1000). Since the particles on the surface are sparse enough, we use the built-in connected components function to obtain the list of particle regions of interest. To discard out-of-size range segmentation, we threshold the connected areas depending on the expected sample size. We then calculate the summation of the absolute photothermal signal at each particle region. We reiterate this process over the whole spectral range. The low SNR signal

particles are filtered at the output spectrum.

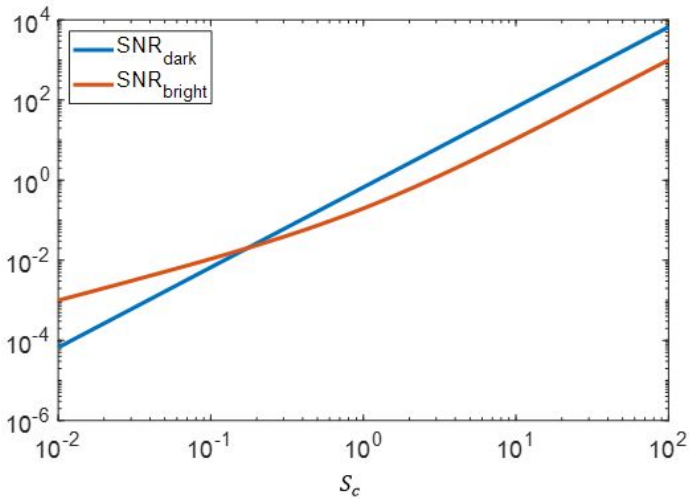

Figure S1: SNR in dark-field and bright-field detection as a function of $S_c = |E_{scat}|/|E_{refl}|$. In all conditions, it is assumed that number of reflected photons $|E_{refl}|^2$ is 20 ke- and $M_{scat} = \Delta|E_{scat}|/|E_{scat}^{cold}|$ is set to 0.0005, and other noise is 30 e-.

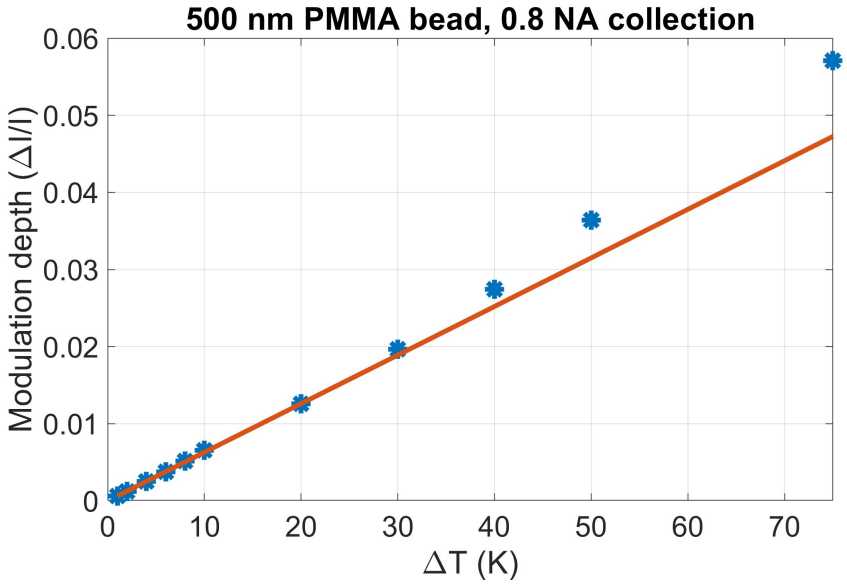

Figure S2: Simulated temperature dependence of photothermal signal for 500 nm PMMA bead. Simulation parameters at 520 nm illumination wavelength: $\theta_{\text{incident}} = 0°$, $n_{\text{medium}} = 1$, $n_{\text{silicon}} = 4.2$, $_{\text{glass}} = 1.5$, $n_{\text{PMMA}} = 1.49$, $dn/dT = -1.1 \times 10^{-4}$ K^{-1}, $dr/dT = 90 \times 10^{-6}$ K^{-1}, $T_0 = 298$ K.

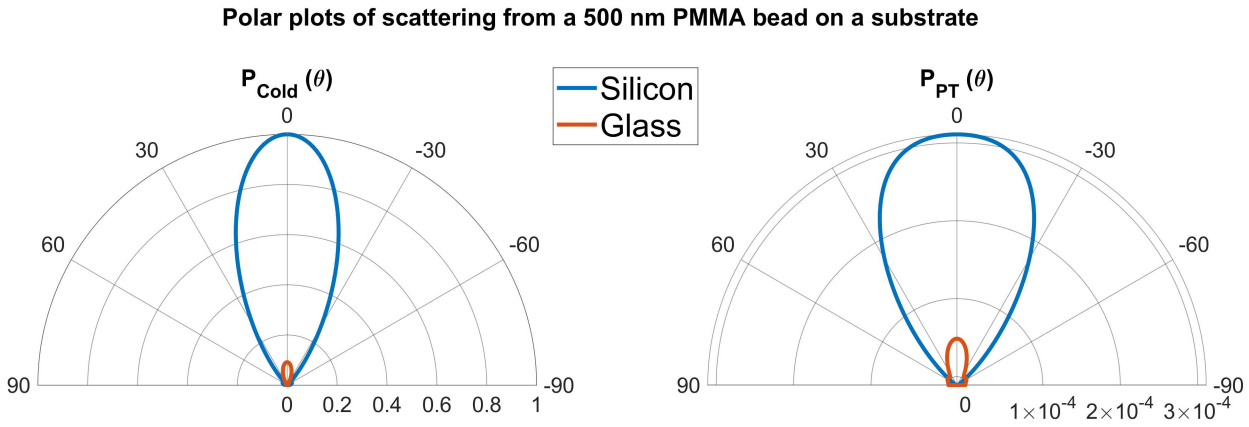

Figure S3: Scattering polar plot comparison of 500 nm PMMA bead on silicon and glass substrates. (Left) DC polar plots normalized with maximum power on the silicon substrate and (Right) photothermal polar plots calculated from the normalized signals. The simulation parameters: $\theta_{\text{incident}} = 0°$, $n_{\text{medium}} = 1$, $n_{\text{silicon}} = 4.2$, $n_{\text{PMMA}} = 1.49$, $dn/dT = -1.1 \times 10^{-4}$ K^{-1}, $dr/dT = 90 \times 10^{-6}$ K^{-1}, $T_0 = 298$ K.

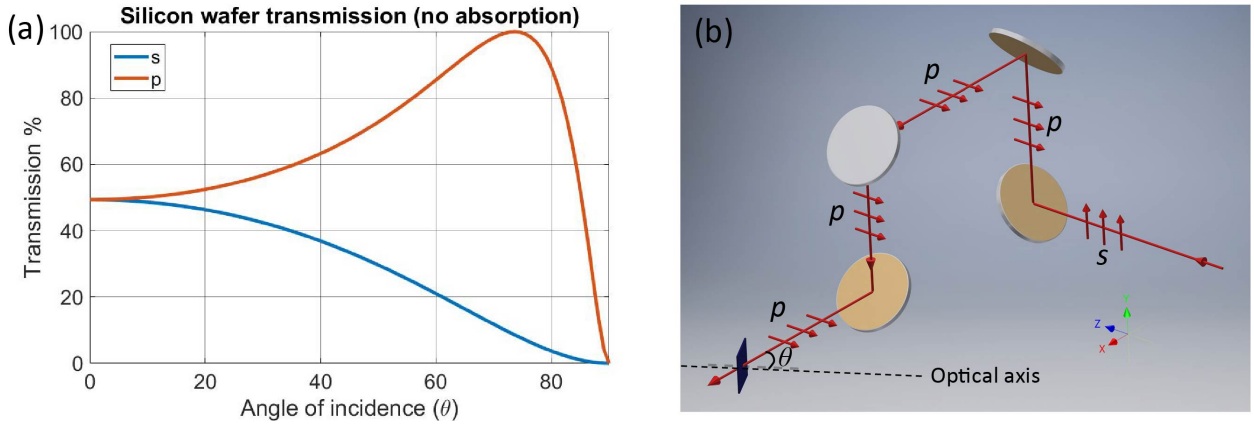

Figure S4: (a) Calculated transmission of silicon substrate for polarized IR beam at various angle of incidence. Simulation parameters: $\tilde{\nu}_{\text{illumination}} = 1650\ \text{cm}^{-1}$, $\text{n}_{\text{silicon}} = 3.4$, $\text{n}_{\text{medium}} = 1$. The imaginary part of silicon refractive index is omitted in the transmission calculations. (b) Topological polarization rotation of IR light from s to p polarization state.

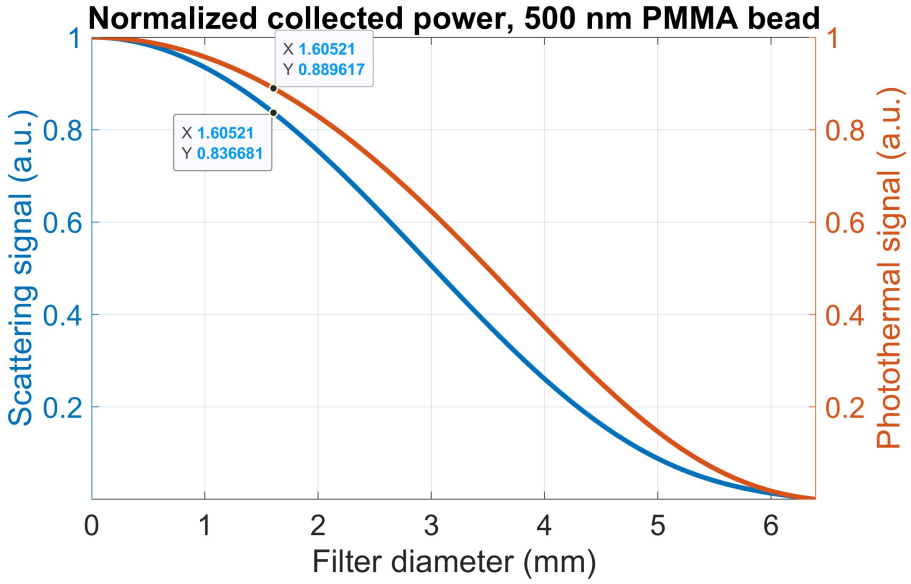

Figure S5: Effect of the blocker size on the collected scattering and photothermal signal power. The scattered intensity is calculated by BEM simulations of 500 nm PMMA bead on silicon. The total collected power is then calculated by numerically taking the spherical integrals within the angular range of the objective numerical aperture. The blocker diameter D can be converted into the blocked NA using numerical aperture equation ($D \approx 2fNA_{block}$). Our objective has 6.4 mm pupil diameter with 4 mm focal length and 0.8 NA. The simulation parameters: $\theta_{\text{incident}} = 0°$, $\text{n}_{\text{medium}} = 1$, $\text{n}_{\text{silicon}} = 4.2$, $\text{n}_{\text{PMMA}} = 1.49$

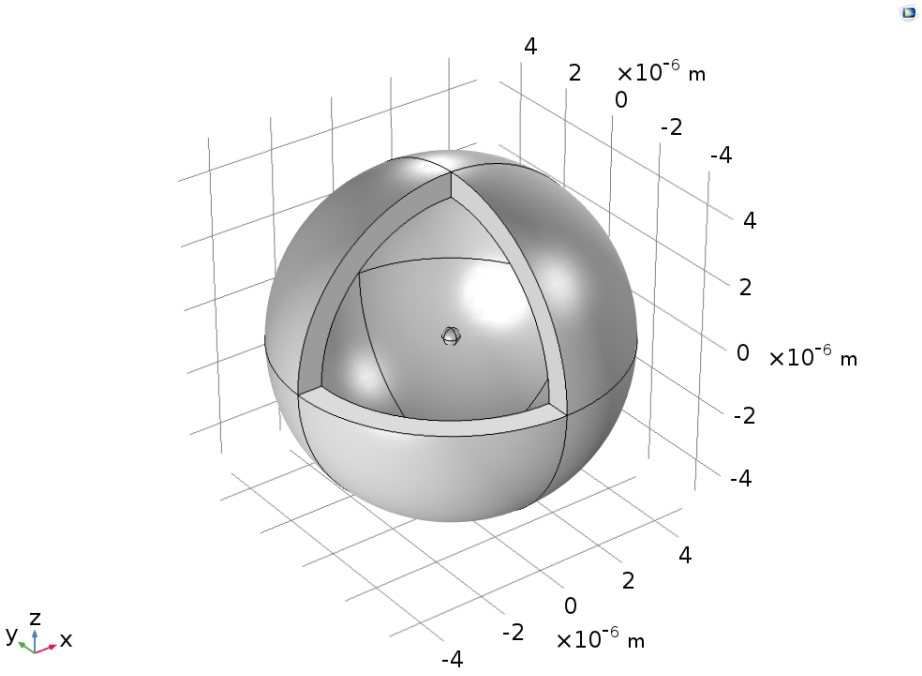

Figure S6: The geometry diagram for the absorption cross section simulation. The center part is the PMMA bead with certain diameter. The surrounding part is air with a 20 times larger diameter of the bead.

Diameter/nm	$\sigma_{abs\_COMSOL}/\mu m^2$	$\sigma_{abs\_Mie}/\mu m^2$
100	3.8901×10^{-4}	3.8859×10^{-4}
200	3.1285×10^{-3}	3.1248×10^{-3}
300	1.0645×10^{-2}	1.0632×10^{-2}
500	5.0447×10^{-2}	5.0390×10^{-2}
1000	4.3436×10^{-1}	4.3396×10^{-1}
2000	3.4489	3.4449

Figure S7: Comparison between the COMSOL simulation and Mie scattering calculator results of absorption cross sections of PMMA beads with different sizes

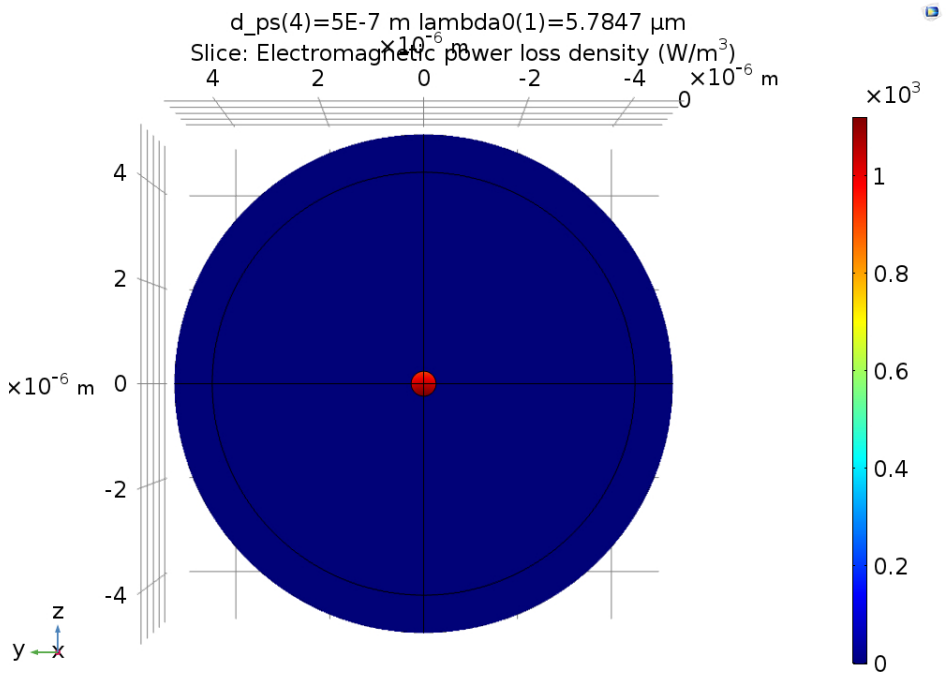

Figure S8: COMSOL simulation result of the electromagnetic power loss density distribution of a 500 nm PMMA bead when heated by a 1729 cm^{-1} electromagnetic wave.

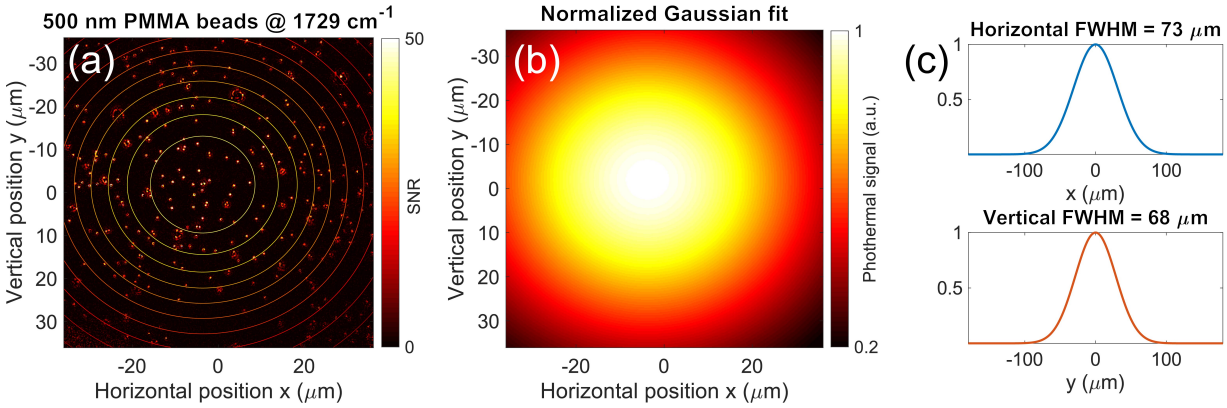

Figure S9: (a) Photothermal signal of 500 nm PMMA beads and mesh plot of IR beam's 2D Gaussian fit ($y = \alpha e^{-ln(2)\cdot(\frac{x^2}{\sigma_x}+\frac{y^2}{\sigma_y})}$). The obtained fitting parameters are $\alpha = 45.27$ (is only an arbitrary number, not the real value of intensity), $\sigma_x = 36.5\mu m$, and $\sigma_y = 33.8\mu m$. (b) Normalized fitted Gaussian beam profile and (c) cross-section across the (top) horizontal and (bottom) vertical directions. The FWHM of IR beam is 73 µm ×68 µm. IR power: 6 mW @ 1729 cm^{-1}, camera FPS: 400 Hz, $N_{avg} = 1000$, image acquisition time: 5 s

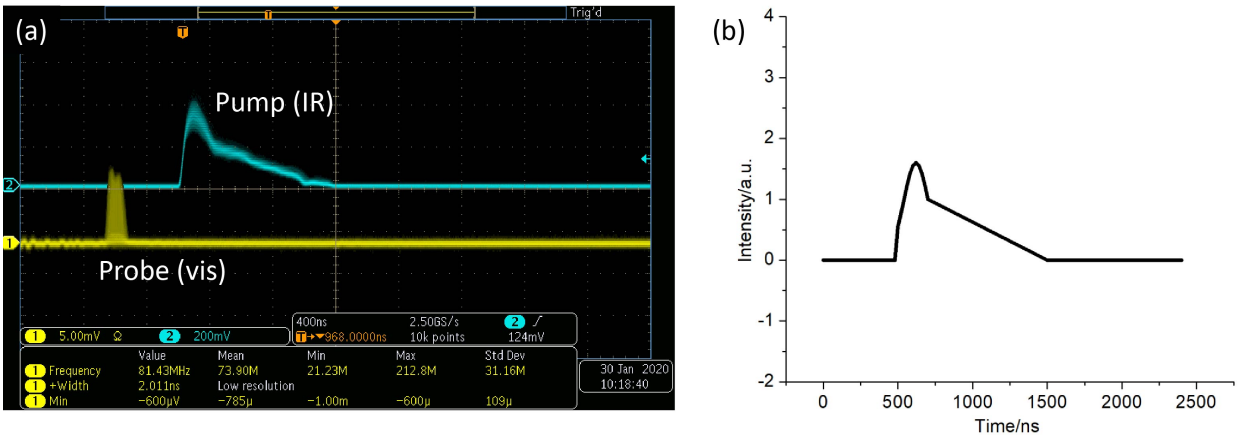

Figure S10: (a) Oscilloscope image of the (blue curve) IR pulse shape at $\tilde{\nu}_{pump} = 1729\ cm^{-1}$ and (yellow curve) visible probe pulse $\lambda = 520$ nm. (b) IR pulse curve fitting obtained by a piecewise function ($\alpha e^{-\frac{1}{2}(\frac{t-\tau_1}{\sigma})}$, for 500 ns $<$ t $<$ 700 ns; $1 - \frac{t-\tau_2}{\tau_3}$, for 700 ns $<$ t $<$ 1500 ns; 0, for otherwise). The fitting parameters are $\alpha = 1.6$, $\tau_1 = 620$ ns, $\sigma = 82.51$ ns, $\tau_2 = 700$ ns, $\tau_3 = 800$ ns.

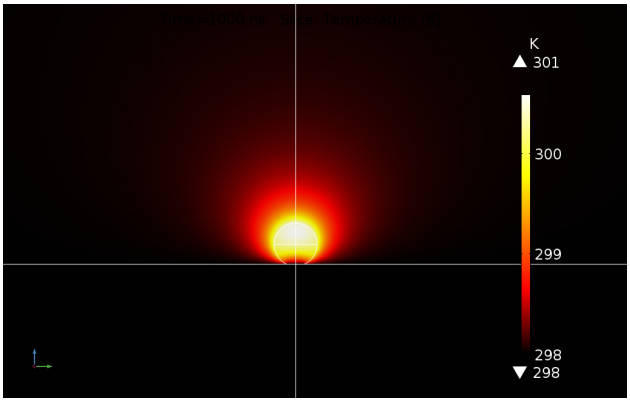

Figure S11: The temperature distribution when the 500 nm PMMA bead is heated by the IR pulse. Time is at 500 ns after the rising edge of the IR pulse.

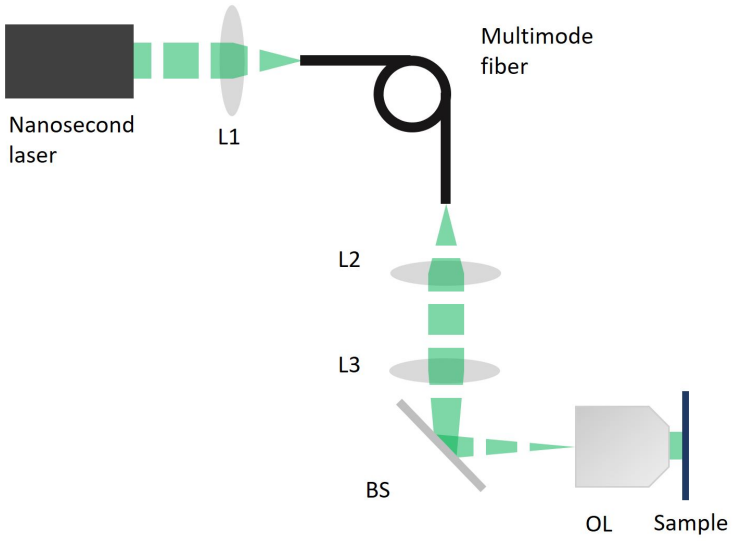

Figure S12: The alternative probe beam for reducing laser speckle in cell imaging. Nanosecond laser: NPL52C, Thorlabs. L1: f = 6.24 mm, C110TMD-A, Thorlabs. Multimode fiber: M102L05, 150 µm x 150 µm Core, Thorlabs. L2: f = 6.09 mm, F110SMA-532, Thorlabs. L3: f = 250 mm, AC254-250-A-ML, Thorlabs. BS: beam-splitter. OL: objective lens. The nanosecond laser is triggered by the pulse generator at 50 kHz and its pulse width is set to 120 ns. The pulse generator channel triggering QCL is set to be 125 on and 125 off. The channel triggering camera is set to be 1 on and 124 off and the camera frame rate is 400 fps. Other parts in the setup are same as illustrated in Figure 2.

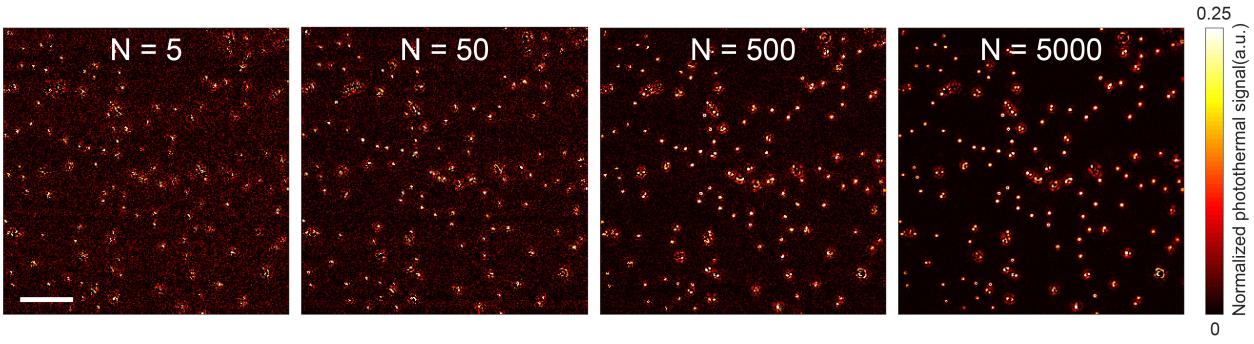

Figure S13: Photothermal signal of 500 nm PMMA beads at different number (N) of averaged frames. IR power: 6 mW @ 1729 cm^{-1} vibrational peak of the C=H bond, camera FPS: 400 Hz, scale bar: 10 µm.

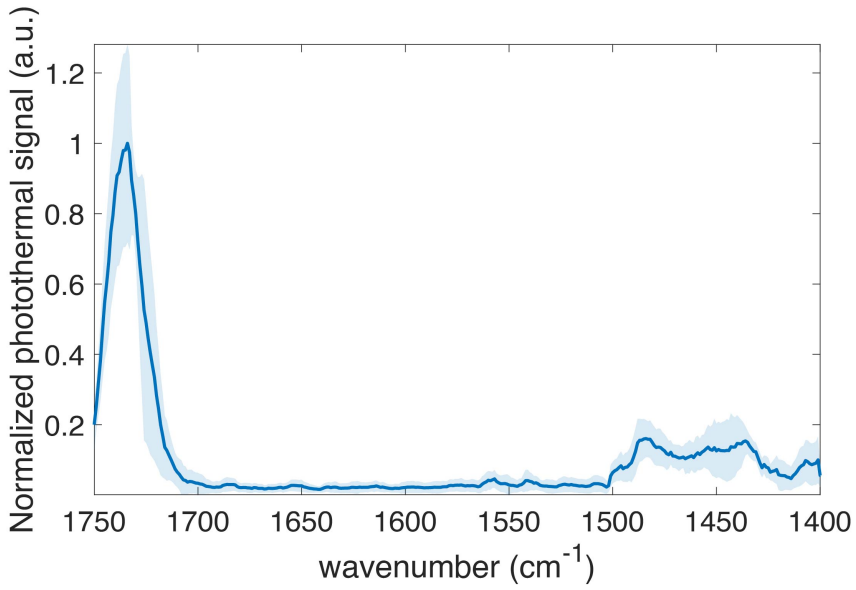

Figure S14: **Spectrum of 20 individual 500 nm PMMA beads** Photothermal image acquisition time at each wavenumber: 5 s. Total scan time: $\sim$ 29 mins

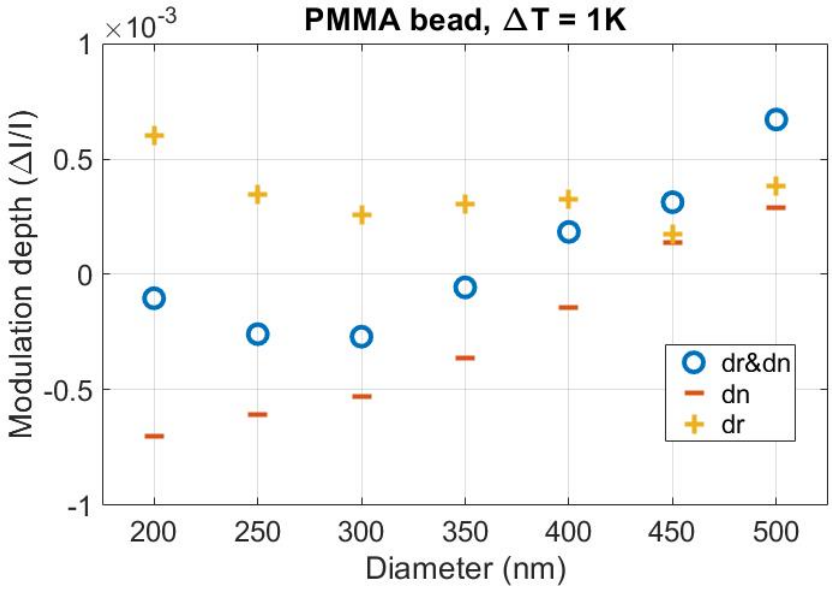

Figure S15: **Simulations for size dependence of photothermal signal for a PMMA bead on the silicon substrate.** The thermal expansion and thermo-optical effects are evaluated separately. Simulation parameters: $\theta_{\text{incident}} = 0°$, $n_{\text{medium}} = 1$, $n_{\text{silicon}} = 4.2$, $n_{\text{PMMA}} = 1.49$, $dn/dT = -1.1 \times 10^{-4}$ K^{-1}, $dr/dT = 90 \times 10^{-6}$ K^{-1}, $T_0 = 298$ K.

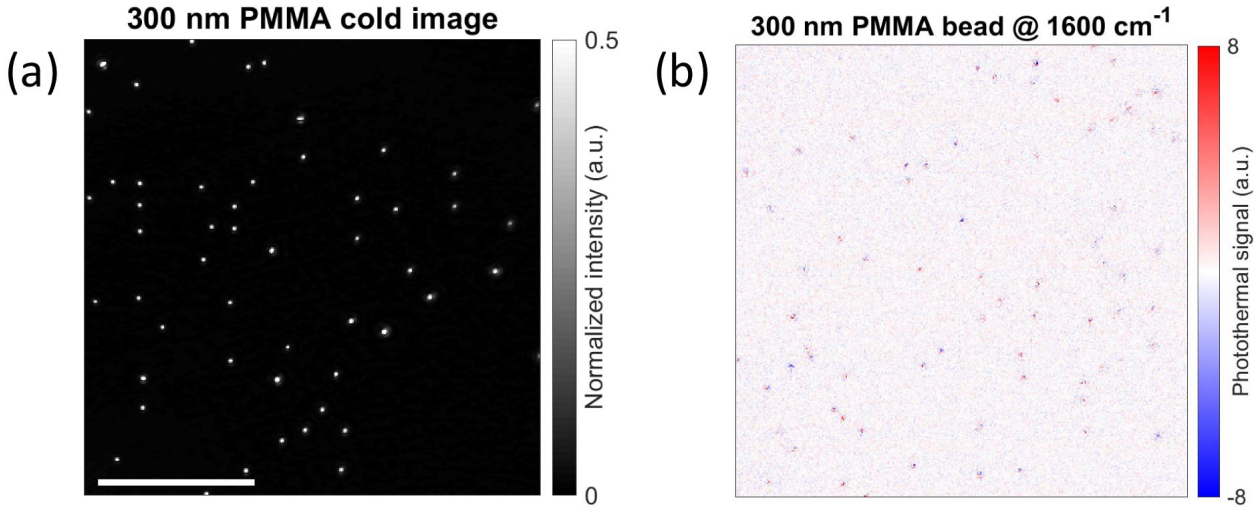

Figure S16: (a) Cold and (b) off-resonance photothermal images of 300 nm PMMA beads. The IR wavelength is tuned to 1600 cm^{-1}. Photothermal image acquisition time: 25 s. Scale bar: 20 µm.

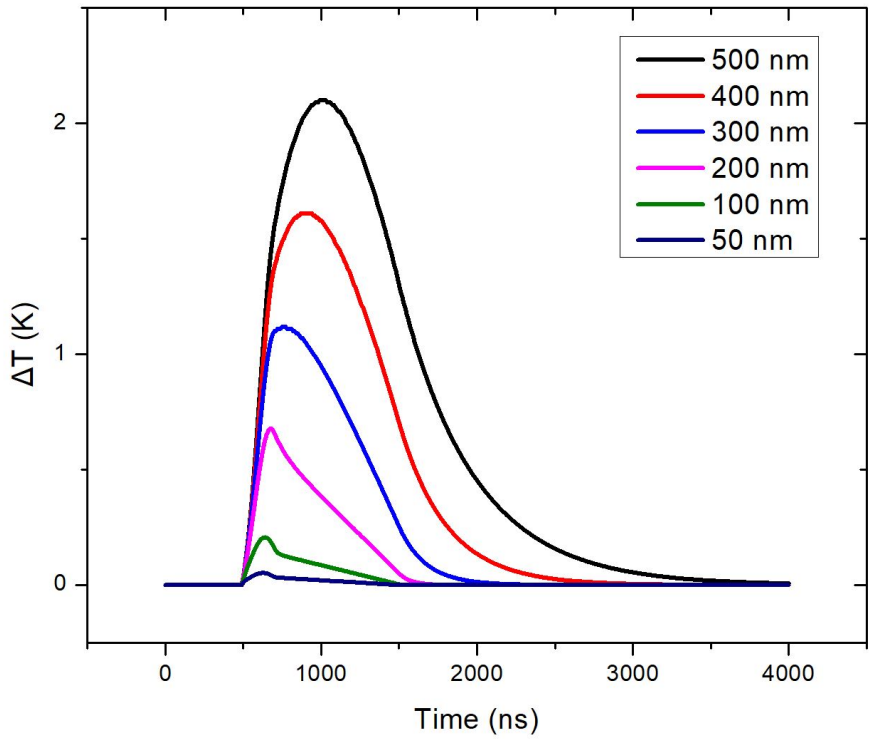

Figure S17: **Temperature rising for different sizes of PMMA beads** The simulation uses the same parameter as the simulation for 500 nm PMMA bead introduced in previous sections.

REFERENCES

(S1) Mark, J. E., et al. *Physical properties of polymers handbook*; Springer, 2007; Vol. 1076.

(S2) Li, Z.; Aleshire, K.; Kuno, M.; Hartland, G. V. Super-Resolution Far-Field Infrared Imaging by Photothermal Heterodyne Imaging. *J. Phys. Chem. B* **2017**, *121*, 8838–8846.

(S3) Tsuda, S.; Yamaguchi, S.; Kanamori, Y.; Yugami, H. Spectral and Angular Shaping of Infrared Radiation in a Polymer Resonator with Molecular Vibrational Modes. *Opt. Express* **2018**, *26*, 6899–6915.